Journal of Materials Chemistry A

PAPER

View Article Online
View Journal | View Issue

Cite this: J. Mater. Chem. A, 2016, 4, 16454

Hierarchical TiO_2 spheres assisted with graphene for a high performance lithium–sulfur battery†

Lin Gao,[a] Minglei Cao,[a] Yong Qing Fu,[b] Zhicheng Zhong,[c] Yan Shen[a] and Mingkui Wang*[a]

Received 25th July 2016
Accepted 15th September 2016

DOI: 10.1039/c6ta06285g

www.rsc.org/MaterialsA

In this study, we report hierarchical TiO_2 sphere–sulfur frameworks assisted with graphene as a cathode material for high performance lithium–sulfur batteries. With this strategy, the volume expansion and aggregation of sulfur nanoparticles can be effectively mitigated, thus enabling high sulfur utilization and improving the specific capacity and cycling stability of the electrode. Modification of the TiO_2–S nanocomposites with graphene can trap the polysulfides *via* chemisorption and increase the electronic connection among various components. The graphene-assisted TiO_2–S composite electrodes exhibit high specific capacity of 660 mA h g^{-1} at 5C with a capacity loss of only 0.04% per cycle in the prolonged charge–discharge processes at 1C.

Introduction

There has been a strong demand for sustainable, renewable energy technologies due to air pollution and global warming. Among the available energy storage methods, rechargeable Li-ion battery represents the state-of-the-art technology in the market. Lithium–sulfur (Li–S) battery is of great interest as a next-generation energy storage solution, particularly for electric vehicles. The ultra-high theoretical energy density (2600 W h kg^{-1}) of the Li–S battery is due to the very high specific capacity of sulfur (1675 mA h g^{-1}) based on a two-electron reaction ($S + 2Li^+ + 2e^- \leftrightarrow Li_2S$).[1–3] Currently, Li–S batteries suffer from a problem of short cycle-life, which could be caused mainly by a coupled 'chemical' and 'mechanical' degradation of polysulfides during the charge–discharge processes.[4–8] When elemental sulfur reacts with lithium ions to form Li_2S, the intermediate polysulfide species (Li_2S_n, $4 \leq n \leq 8$) are formed, which are soluble in most electrolyte solutions. The polysulfide intermediates are gradually dissolved in organic electrolytes and shuttle between the anode and cathode, leading to the deposition of insoluble and insulated Li_2S and Li_2S_2 on both the electrodes. This will prevent further lithiation/delithiation processes, eventually causing severe capacity loss.[9,10] In addition, the low conductivity (5×10^{-30} S cm^{-1}) of sulfur at room temperature and ~76% volume expansion/contraction during operation of the conversion reaction ($S_8 \leftrightarrow Li_2S$) result in low utilization efficiency and poor rate performance in the charge–discharge processes.[11–13]

To solve the abovementioned issues, a holistic research approach is needed to radically extend the cycle life and performance of Li–S batteries. For example, the discharge products Li_2S_2/Li_2S with intrinsic insulating properties limit the devices' high-rate operation. Carbon frameworks with good electronic conductivity and copious pores have been regarded as one of the preferred carriers to support sulfur, including double-shell and hollow carbon spheres,[14] fibrous hybrids of graphene,[15–19] conductive polymer such as polyaniline coated carbon nanosphere,[20] nano-graphene sheets.[21] A substantial amount of sulfur can be effectively constrained in these conductive frameworks due to large surface area and pore volume. Interestingly, three-dimensional porous graphitic carbon composites were suggested to have the capability of increasing the sulfur content up to 90 wt%.[22] Because of high sulfur content, good distribution of sulfur nanoparticles, and covalent bonding between sulfur and porous graphitic carbon, the developed cathodes exhibit excellent performance with a high sulfur utilization, high specific capacity, and excellent rate capability at a high charge/discharge current. A large specific capacity in the range of 1000–1200 mA h g^{-1} at a low current rate with a superior cycling stability could be achieved for these electrodes. This is due mainly to a rational design, which efficiently minimizes the polysulfide diffusion into electrolytes. Nevertheless, there is weak physical absorption between the non-polar carbon materials and polar polysulfide intermediates, which causes inefficient prevention of the

[a]Wuhan National Laboratory for Optoelectronics, Huazhong University of Science and Technology, Luoyu Road 1037, Wuhan 430074, China. E-mail: mingkui.wang@mail.hust.edu.cn

[b]Department of Physics and Electrical Engineering, Faculty of Engineering and Environment, Northumbria University, Newcastle Upon Tyne, NE1 8ST, UK

[c]Hubei Key Laboratory of Low Dimensional Optoelectronic Material and Devices, Hubei University of Art and Science, Longzhong Road 296, Xiangyang, 441053, China

† Electronic supplementary information (ESI) available: SEM image and corresponding EDS mapping of TiO_2–S electrode; TEM image of an individual TiO_2 nanoflake; photographs of the disassembled cells corresponding to the CS, TS, and GTS electrodes. See DOI: 10.1039/c6ta06285g

detachment of sulfides and serious degradation problems over long-term cycling.[23,24]

To date, metallic oxides, such as TiO_2 and MnO_2, have been proven to be effective in inhibiting polysulfide dissolution processes, which is favorably comparable with the conventional carbon materials.[25] In particular, TiO_2 could be one of the strong candidates for impregnation of sulfur due to its low-cost and facile fabrication process as well as nontoxicity.[8,26] For example, sulfur–TiO_2 yolk–shell nano-architectures were used as the cathode for an Li–S battery, exhibiting a minor capacity decay of 0.033% per cycle undergoing 1000 cycles at 0.5C.[26] The hierarchical TiO_2 spheres, being in possession of polar surface, could strongly bind polysulfides, delivering a high reversible capacity of 928.1 mA h g^{-1} after 50 charge–discharge cycles at a current density of 200 mA g^{-1}.[27] Fundamentally, such improvements present a materials science and manufacturing challenge: normally, metal oxides have relatively low electronic conductivity.[28] Accordingly, various strategies have been proposed by combining carbon materials with TiO_2 to efficiently promote both the TiO_2 electronic conductivity and the binding between polysulfides and cathode.[29–31] For instance, a graphene–TiO_2 composite was designed to confine sulfur.[29] Electrochemical characterization revealed that the graphene–TiO_2–S sandwich electrode could deliver an enhanced cycling stability with a capacity of 737 mA h g^{-1} (along with a capacity retention of 75%) after 100 cycles at 1C, due to the highly conductive graphene layers, which facilitate the transportation of electrons.[29] Another design was proposed by Hwang *et al.* to confine sulfur within hollow-mesoporous and spherical TiO_2 particles that are interconnected *via* multi-walled carbon nanotubes.[32] The hollow nanostructure and large pore volume of the spherical TiO_2 particles provide sufficient accommodation for the volume expansion of sulfur. Consequently, the electronic conductivity of TiO_2 and Li^+ ion diffusion can be improved effectively by multiple pathways in a web of carbon nanotubes. An ultra-high capacity of 931 mA h g^{-1} at 5C was achieved with this electrode.

Based on previously reported results, in this study, we presented a new protocol for high performance Li–S battery using an interconnected architecture based on graphene-modified TiO_2 spheres frameworks. Rather than the hollow TiO_2 and TiO_2 nanoparticles, we for the first time investigated hierarchical TiO_2 spheres combined with graphene utilized as the sulfur host for the Li–S battery. With this strategy, the sulfur nanoparticles can be distributed uniformly inside the hierarchical TiO_2 spheres, which efficiently mitigate sulfur aggregation and volume expansion, and thus improve sulfur utilization.[33–36] More importantly, the modification of graphene layers can not only increase the electrode's electronic conductivity, but also effectively form a shield to prevent the polysulfides from detaching and being released into the electrolytes. The assembled Li–S cells show stable cycling performance with only a capacity loss of 0.04% per cycle in the prolonged charge–discharge processes (400 cycles at 1C). This newly proposed structural design allows a significant improvement in the cycle life performance wherein the battery can be charged/discharged without significantly losing its capacity. Therefore, this provides a new solution for one of the major issues of rapid degradation of cathode performance for Li–S batteries.

Experimental section

Material synthesis

The hierarchical TiO_2 spheres were prepared as follows.[37] 1 mL tetrabutyl titanate (TBT) was added into 50 mL acetic acid (HAC) under mild magnetic stirring, followed by a hydrothermal reaction inside a 90 mL polytetrafluoroethylene vessel at 150 °C for 8 hours. After being centrifuged using water, the products were dried at 80 °C in an oven and calcined at 400 °C for 1 hour to obtain the well-crystallized anatase TiO_2. Sulfur powder (from Sinopharm Chemical Reagent Co., Ltd., Shanghai, China) was thoroughly mixed with the synthesized TiO_2 at a weight ratio of 2.5 : 1. The compounds were placed into a polytetrafluoroethylene vessel (10 mL) and heated to 200 °C for 12 hours, and sulfur was melted and diffused into hierarchical TiO_2. The obtained products are denoted as TS (short term for TiO_2–sulfur sample). Graphene oxide (GO) was fabricated according to reported procedure.[38] GO with a concentration of 0.5 g mL^{-1} was sonicated for 1 hour to obtain a uniform solution with a dark grey color. Then, 30 mg TS was added to the solution to homogeneously blend with GO *via* continuous sonication for 30 min. 18 μL hydrazine hydrate and 126 μL $NH_3 \cdot H_2O$ were added into the solution in a sealed glass bottle to reduce GO at 90 °C for 1 hour.[39] Through this reduction process, the color of the solution gradually changed into black, demonstrating the successful reduction of GO to graphene. After centrifugation for three times, the solution was dried at 60 °C for 12 hours and the final product was obtained, which is denoted as GTS. On the other hand, sulfur and carbon hybrid sample (CS) were prepared superlatively. Carbon black and sulfur powders with a mass ratio of 2.5 : 1 were ground together in a mortar, and then heated at 200 °C for 12 hours and then dried at 60 °C for 48 hours.

Fig. 1 presents the fabrication process of the graphene-modified TiO_2–S composite (*i.e.* the GTS). First, the hierarchical TiO_2 nanostructures were fabricated based on the hydrothermal reaction using tetrabutyl titanate (TBT) as the precursor together with acetic acid. The sulfur powders were then mixed thoroughly with TiO_2 and held in a sealed container at 200 °C for 12 hours. In this process, melted sulfur was fully infiltrated into the inner nanostructures of TiO_2. Furthermore, the TS composite was successfully encapsulated with graphene *via* the *in situ* reduction reaction (as illustrated in the synthesis process of the GTS in Fig. 1).

Characterization

Field-emission scanning electron microscopy (FE-SEM, Nova Nano 450, Netherlands) and energy dispersive X-ray spectroscopy (EDS) were used to observe the morphology of the obtained materials. The porous structures and lattice fringes were further determined utilizing a transmission electron microscope (TEM, Tecnai G220). Crystalline structures of the materials were analyzed using an X-ray diffractometer (XRD, X'Pert PRO,

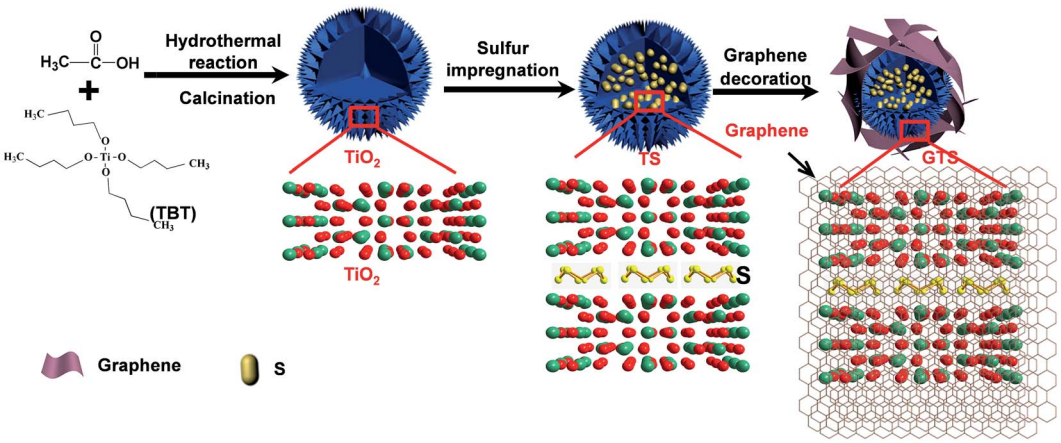

Fig. 1 Schematic of the fabrication of the hierarchical TiO_2, TiO_2–S (TS), graphene-modified TiO_2–S composite (GTS). To clearly illustrate the distribution of sulfur particles in the hierarchical TiO_2 spheres, a hollow-structure design is used to describe the inner structure for TiO_2–S sample.

PANalytical B.V., Netherlands) with Cu Kα1 irradiation (λ = 1.5406 Å). X-ray photoelectron spectroscopy (XPS, AXIS-ULTRA DLD-600W) was used to examine the surface chemical nature of the GTS.

Thermogravimetry (TG) combined with thermogravimetry and differential scanning calorimetry measurements (TGA-DSC) (PerkinElmer Diamond) in N_2 were conducted to characterize the actual mass ratio of sulfur in the TS and GTS powders. Raman spectroscopy (LabRAM HR800, Horiba) was carried out to reveal the chemical property of the encapsulated graphene. The mean pore size distributions and the specific Brunauer–Emmett–Teller (BET) surface areas of TiO_2 were obtained with accelerated surface area and porosimetry based on N_2 isotherm adsorption/desorption measurement (Micromeritics ASAP 2020, US).

Electrochemical test

In a standard electrochemical measurement, the CS, TS and GTS samples were mixed thoroughly with polyvinylidene fluoride (PVDF) and carbon black (with the weight ratio of 8 : 1 : 1). The powders were then dissolved into *N*-methylpyrrolidone (NMP) solvent and stirred for 12 hours at ambient temperature. The solution was then casting coated onto an Al foil and dried at 80 °C for 12 hours in a vacuum chamber. The mass loading on an Al foil was controlled in the range of 1.5–2 mg cm^{-2} measured using a micro balance (METTLER TOLEDO, XS3DU, Switzerland). The thickness of the film coated on the Al foil was around 42.4 μm according to SEM (data not shown). Coin-type cells were assembled to evaluate the electrochemical performance of the as-derived materials and the capacity was calculated based on the mass of sulfur.

The tested electrodes were assembled to 2016 half cells using an Li foil as a counter electrode, and a porous polypropylene membrane as a separator. The device fabrication was carried out in an Ar-filled glove-box, in which the moisture and oxygen contents were less than 1 ppm. The electrolytes were composed of lithium bis-(trifluoromethanesulfonyl)imide (LiTFSI, 1 M) in a mixed solvent of 1,3-dioxolane and 1,2-dimethoxyethane (volume ratio 1 : 1) combined with lithium nitrite (1 wt%). The electrochemical performance of the prepared electrodes was evaluated using a Landbattery system (CT 2001A Wuhan, China) with the voltage range of 1.5–2.8 V (*vs.* Li^+/Li) at various current densities. Cyclic voltammetry (CV) and electrochemical impedance spectroscopy (EIS) were conducted using a CHI 660D electrochemical workstation.

Results and discussion

Fig. 2a displays a typical SEM image of the prepared hierarchical TiO_2 spheres with an average diameter of ~3–4 μm. The hierarchical TiO_2 spheres consist of overlapped subunit of nanoflakes, which lead to a large surface area and a uniform distribution of pore sizes. After the adequate impregnation of sulfur, the ultra-thin nanoflakes of TiO_2 disappeared due to an even infiltration of sulfur (see Fig. 2b). The intimate decoration of graphene on the TS composite can be verified from the layered architecture with spherical morphology, as illustrated in Fig. 2c. EDS analysis (see Fig. 2d) demonstrated the existence sulfur by a strong peak at energy of ~2.3 keV in the GTS sample. In addition, a homogeneous distribution of sulfur nanoparticles within the TS (Fig. S1†) and GTS (Fig. 2e) samples can be further confirmed by EDS mapping analysis, which also verifies that introduction of graphene in the GTS has a minor influence on the uniform distribution of sulfur inside the TiO_2 spheres. Fig. 2f compares the XRD patterns of the TiO_2, TS and GTS powders. Apart from the peaks at 25°, 38° and 48° for the (101), (004) and (200) phases of anatase TiO_2 from the well-crystallized TS and GTS, the remaining peaks can be assigned to orthorhombic sulfur (JCPDS no. 08-0247). The sulfur content in various samples was measured by TGA, as shown in Fig. 2g. The TGA plot shows 70.5 wt% weight loss between 100 °C and 320 °C and 55 wt% weight loss (Fig. S2†) between 100 °C and 295 °C for the TS and GTS samples, respectively. This corresponds to the release of sulfur that was presented in the TS and GTS samples. The 55 wt% sulfur in the GTS sample corresponds to a sulfur

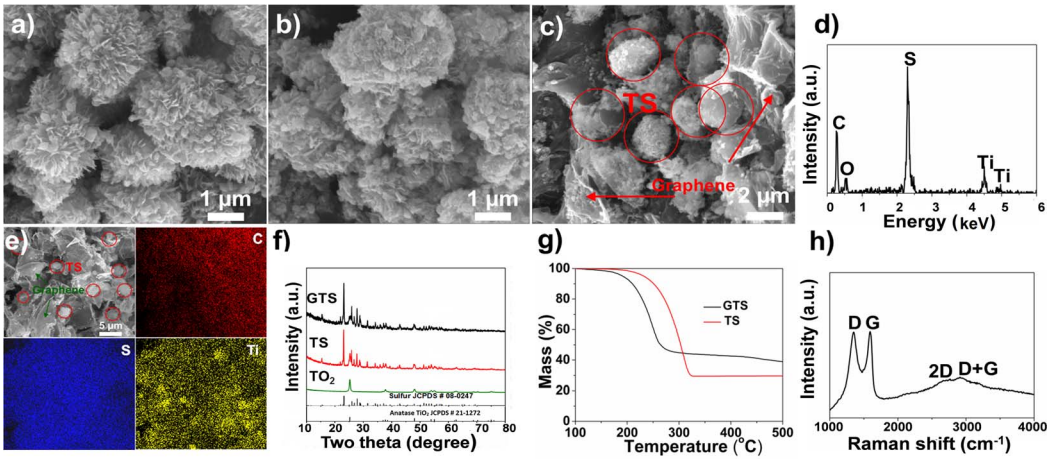

Fig. 2 SEM images of (a) the hierarchical TiO_2, (b) the TiO_2–S (TS) and (c) the graphene-modified TS composite (GTS); (d) the corresponding EDS analysis for the GTS; (e) the EDS mapping for C, S, Ti for the GTS; (f) XRD patterns of the GTS, TS and TiO_2 samples; (g) thermogravimetry analysis (TGA) curves of the GTS and TS samples in nitrogen. (h) Raman spectroscopy result of the GTS sample.

loading of ~1.0 mg cm^{-2} in the cathode. Notably, there are two step mass losses for the GTS sample in the TGA test. The weight loss between 295 °C and 500 °C could be attributed mainly to the pyrolysis of oxygen-containing functional groups of graphene in GTS.[40,41] The presence of graphene in the final GTS sample can be identified easily by X-ray photoelectron spectroscopy (XPS), as shown in Fig. 2h. Two prominent peaks are observed at 1351.6 cm^{-1} and 1591.8 cm^{-1}, corresponding to the characteristic D and G bands of the graphene in the GTS sample.[17,42] The intensity ratio of the D band to G band (I_D/I_G) is commonly used to evaluate the degree of defects in carbon materials. A higher ratio indicates an increased amount of defects. For the GTS sample, the intensity ratio (I_D/I_G) was calculated to be 1.24, demonstrating the existence of large amounts of defects. This results in an enhanced electronic conductivity related to the sufficient reduction of GO.[17,18]

TEM characterization shown in Fig. 3a and b reveals the hierarchical TiO_2 sphere architecture. Fig. 3a shows the hierarchical TiO_2 spheres of ~3 μm in diameter with a layered nanostructure, which agrees well with the aforementioned SEM images. The thickness of TiO_2 nanoflakes was evaluated to be ~4 nm according to the high magnified TEM images (Fig. 3b). It is noted that there are a plethora of mesopores in the individual TiO_2 nanoflakes (Fig. S3†), which is beneficial for the efficient implantation of molten sulfur and also can effectively reduce the size of sulfur nanoparticles.[40,43] Fig. 3c displays a TEM image of the TS sample. The layered nanostructure clearly disappears after penetration of sulfur. In addition, the higher magnification TEM image in Fig. 3c and the inset reveal numerous dark dots with an average size of 20 nm. This result is different from the inset of Fig. 3b. These can be ascribed to the uniformly distributed sulfur nanoparticles.[44] The corresponding EDS mapping of S, O and Ti within the selected rectangular area in Fig. 3d verifies the uniform distribution of sulfur inside the TS matrix. The TEM observation of the GTS sample in Fig. 3e reveals the successful decoration of the graphene on the TS composites (marked with white circles). This result also indicates good contact between TS and graphene, and a homogenous distribution of the sulfur nanoparticles in both the TS and GTS samples. The layered structure corresponding to graphene can be clearly observed, as shown in Fig. 3f.

The BET-surface area of the TiO_2 sphere was determined to characterize the hierarchical feature of TiO_2 spheres. The adsorption–desorption isotherm curves (see Fig. 4a) of the TiO_2 spheres with typical hysteresis loops indicate the abundant existence of mesopores with two type of pore size distribution centered at 5 nm and 20 nm, respectively (Fig. 4b).[28,45,46] A large BET surface area of 116.6 m^2 g^{-1} and a specific pore volume of 0.55 cm^3 g^{-1} can be determined for the hierarchical TiO_2 spheres, which is beneficial to uptaking sulfur into the nanostructures. Fig. 4c presents the XPS survey spectrum of the GTS powders, revealing the existence of C, Ti, O and S.[35,47,48] The high-resolution C1s XPS spectrum of GTS sample in Fig. 4d can be fitted with four different components of carbon-containing functional groups at binding energies of ~284.9 eV (C–C), ~285.7 eV (C–S), ~287.3 eV (C═O), and ~289.9 eV (O–C═O).[17,19] Among them, the carbonyl (C═O) and carboxyl (O–C═O) groups with weaker peak intensity can be assigned to the remaining GO in GTS without sufficient reduction.[19] The C–S peak can be attributed to the chemical bond between graphene and sulfur formed during the *in situ* reduction process of graphene oxide. This bond is beneficial for hindering polysulfide dissolution, thus improving the cycling performance as discussed below.

Fig. 5a and b present the galvanostatic charge–discharge curves for the TS and GTS electrodes in a potential range of 1.5–2.8 V at different current rates. It was found that the polarization of GTS electrode (Fig. 5a) is much smaller than that of TS electrode (Fig. 5b), even at a higher current density. The GTS electrode deliveries higher specific discharge capacities at high rates, *i.e.*, ~816 mA h g^{-1} at 1C, ~760 mA h g^{-1} at 2C, ~725 mA h g^{-1} 3C, and 660 mA h g^{-1} at 5C. Fig. 5c shows the cycling performance and the derived data of the coulombic efficiency for the CS, TS and GTS electrodes at a current rate of 1C (1C =

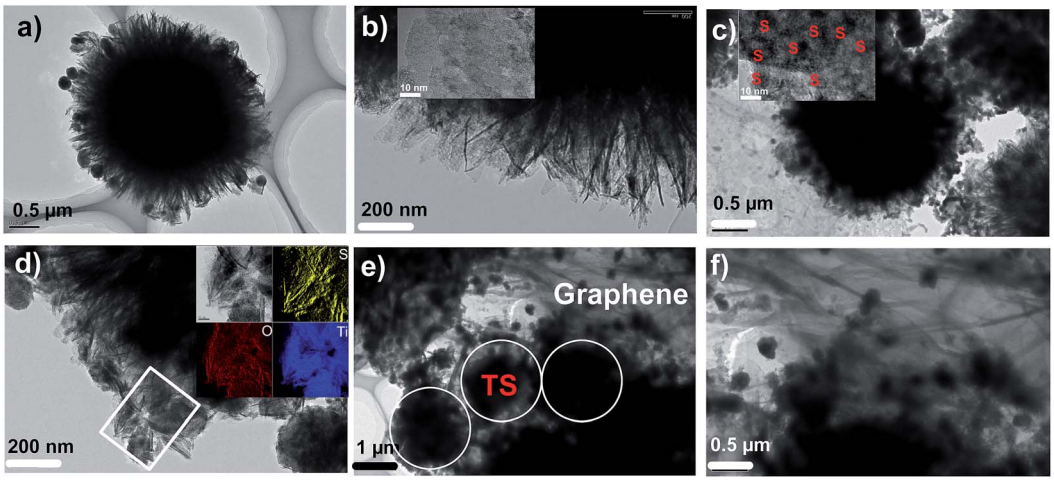

Fig. 3 TEM images for TiO_2, TiO_2–S (TS), graphene-modified TiO_2–S composite (GTS) samples: (a) the low-magnification and (b) high-resolution TEM images of the TiO_2 sphere sample. The inset corresponds to the HRTEM image. (c) Low-magnification and (d) high-resolution TEM images of the TiO_2–S (TS) sample. The inset is the HRTEM image. (d) The enlarged TEM image of (c). The inset is the EDX and elemental analysis result. (e) and (f) are TEM images of the GTS sample.

1675 mA g^{-1}) for 100 cycles. A CS electrode (blue symbol) was provided as the reference data to prove the effective polysulfide entrapment of the designed framework. It can be seen from Fig. 5c that the GTS electrode possesses the most stable cycling performance with remarkable 94.4% capacity retention of the original capacity. In contrast, the CS electrode shows a rapid capacity loss with a low specific capacity of 572.9 mA h g^{-1} after 100 cycles, occupying only 69.9% capacity retention of the original capacity (~821 mA h g^{-1}). The drastic capacity decay for the CS electrode is associated with the significant polysulfide dissolution as a result of the weak interactions between the nonpolar carbon and polar sulfides.[43] The coulombic efficiency of the GTS electrode was estimated to be ~98%, which is much higher than those of the TS and CS electrodes. This can be explained from a minimized shuttle effect and excellent electrochemical reversibility based on the use of the GTS electrode. The synergistic combination of graphene and hierarchical TiO_2 guarantees the excellent cycling performance and high coulombic efficiency of the Li–S battery. Owing to the suitable design of utilization TiO_2 as the sulfur scaffold and graphene as the polysulfide barrier, the two-electron reaction process on the cathode ($S + 2Li^+ + 2e^- \leftrightarrow Li_2S$) can be efficiently reversible with much less polysulfide dissolution, leading to stable cycling performance and high coulombic efficiency. The GTS and TS electrodes were tested continuously for their rate performance after 100 charge–discharge cycles at a constant current rate of 1C. Fig. 5d displays the rate performance for the GTS and the TS electrodes at various current rates. The GTS electrode exhibited a much higher capacity than that of the TS electrode in the entire charge–discharge process. A specific capacity of 660 mA h g^{-1} was obtained for the GTS electrode at a rate as high as 5C. When the current rate was changed back to 1C, a capacity of 800 mA h g^{-1} is remained for the GTS electrode, nearly 100% capacity retention of the original capacity. These results demonstrate an excellent reversibility using the GTS electrode. In addition, the size of hierarchical TiO_2 plays significant role on the electrochemical performance of Li–S batteries. Thus, it is still urgent to optimize the size of TiO_2 host to further enhance their performance. Long-term cycling tests were further carried out for the GTS electrode to verify its electrochemical stability. After 400 cycles at 1C, the electrode still maintained a capacity of 732 mA h g^{-1} (Fig. 5e), being ~83% capacity retention of the primary capacity with a capacity loss of 0.04% per cycle.

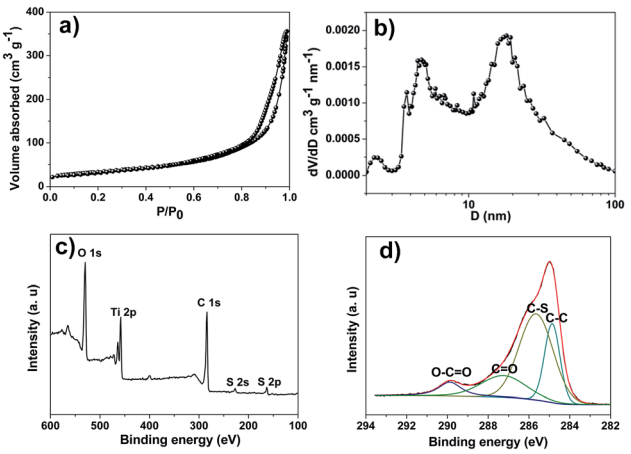

Fig. 4 (a) N_2 adsorption–desorption isotherm profiles and (b) pore size distribution of the TiO_2 sphere sample. (c) XPS survey scan; and (d) high-resolution scan of C1s for graphene-modified TiO_2–S composite sample.

Fig. 6a presents an SEM image of the GTS electrode after charge–discharge process for 400 cycles. A spherical morphology can be observed, which was attributed to the TS microstructure, implying the sturdy structure of the hybrids, which can accommodate the sulfur volume change.[44] The retention of sulfur and its distribution after 400 cycles could be

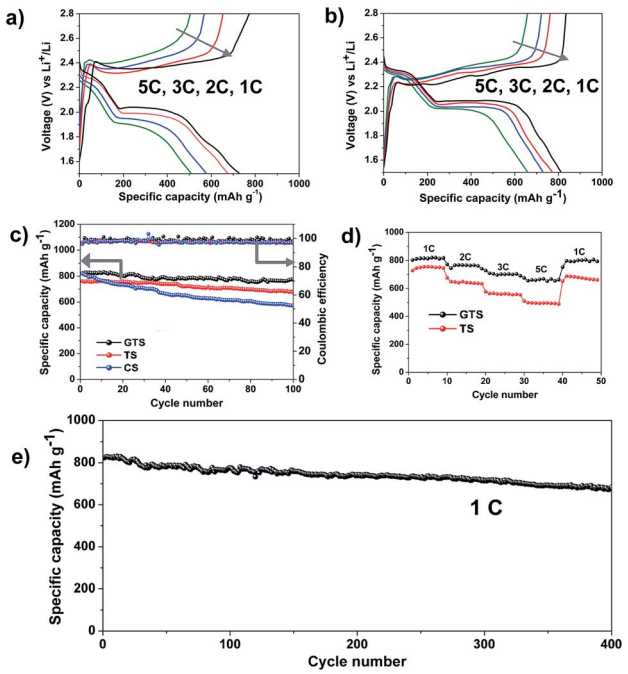

Fig. 5 Galvanostatic charge–discharge curves of (a) TiO_2–S (TS) and (b) graphene-modified TiO_2–S composite (GTS) electrodes. (c) Cycling performance (left coordinate) of the GTS (black symbol), TS (red symbol) and CS (blue symbol) electrodes at 1C and the corresponding coulombic efficiency (right coordinate). (d) Rate performance comparison between TS and GTS electrodes. (e) Cycling performance of the GTS electrode undergoing 400 cycles at 1C.

detected by the EDS characterization of the cycled GTS electrode, as shown in the inset of Fig. 6a. The weak peaks for fluorine can be linked with PVDF.[36] To further verify if there are strong interactions between the GTS cathode and polysulfides, the coin cells made using the CS, TS and GTS electrodes were disassembled to investigate the surfaces of the cathode and counter electrodes (Fig. S4†). The original orange color polysulfides were found to dissolve into electrolytes on the surface of the CS electrode, whereas such phenomena were not observed on the surfaces of both the TS and GTS electrodes. These results reveal that the polysulfide dissolution has been suppressed significantly *via* formation of interconnected

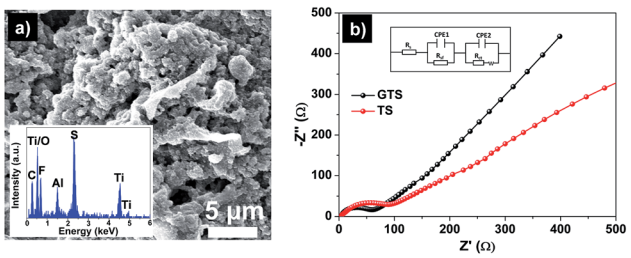

Fig. 6 (a) SEM image of the graphene-modified TiO_2–S composite (GTS) electrode after 400 cycles at 1C and the corresponding EDX spectrum as shown in the inset. (b) Nyquist plots of the GTS and TiO_2–S (TS) electrodes undergoing 100 cycles at 1C (the inset is the equivalent circuit for fitting of the impedance data).

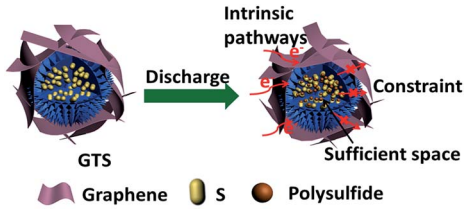

Fig. 7 Schematic of the lithium process in graphene-modified TiO_2–S composite (GTS) sample.

architectures of the graphene-assisted TiO_2–S framework, and a synergistic protection function from both TiO_2 and graphene. Fig. 6b presents the typical Nyquist plots for these electrodes at an open-circuit voltage obtained from impedance measurements. The circuit diagram in the inset is used to simulate the lithium ion transportation process, in which the semicircle and oblique lines are related to the medium and low frequency processes, respectively.[49] The charge transfer resistance (R_{ct}) mostly contributed to the overall resistance for the electrode.[50,51] The value of R_{ct} for the cycled TS and GTS electrodes was calculated to be 103.2 and 47.9 Ω, respectively. The lower value of the resistance for the GTS electrode is attributed mainly to the modification of conductive graphene on the TS surfaces.

The large surface area and abundant mesopores of the TiO_2 sphere can enhance the impregnation of sulfur and can reduce the dimension of the sulfur particles into the nanoscale during the melt infiltration. These can significantly prevent the volume expansion and improve the sulfur utilization rate.[52] In addition, TiO_2 may also take part in the electrochemical reaction, which could make a contribution to the improvement of the capacity for GTS and TS electrodes.[53–56] Furthermore, the modification of graphene for the TS microstructures plays an important role in improving the cycling performance and rate capability. Therefore, based on the schematic shown in Fig. 7, we can conclude that the interconnected frameworks provide (a) a good modification of conductive graphene on the hierarchical TiO_2, (b) the multi-pathways for Li^+ ions diffusion, and (c) the conductive networks for electron transfer. Furthermore, the chemical bond between graphene and sulfur, together with the adsorption of graphene to sulfur and polysulfides due to the existence of many contact sites, can prevent the loss of sulfides during charge/discharge processes. In brief, the synergistic effects from both TiO_2 and graphene stabilize sulfur and polysulfides and promote the efficient transportation of electrons and lithium ions, thus providing stable cycling performance and a high coulombic efficiency using the GTS cathode.

Conclusions

Graphene-assisted TiO_2–S interconnected frameworks were successfully designed, fabricated and used as the cathode materials for Li–S batteries. The hierarchical architectures of TiO_2 sphere with overlapped subunits of nanoflakes can effectively accommodate sulfur nanoparticles. Therefore, the volume expansion and nanoparticle aggregation can be effectively mitigated, thereby facilitating the sulfur utilization rate.

Further modification of graphene for the TS composite can not only improve the electronic conductivity, but also significantly provide the effective pathways for the Li^+ ions and electrons and suppress the diffusion of polysulfides to electrolytes, thus providing excellent cycling stability and high coulombic efficiency. In addition, the chemical bond detected in the GTS products between graphene and sulfur can efficiently stabilize polysulfides on the cathode. The GTS electrodes exhibit appreciated performance, even though the sulfur content in this type electrode is relative low. Therefore, it is highly desirable to optimize the electrode composition to further enhance their performance.

Acknowledgements

Financial support from the China Scholarship Council (no. 201506165038), the Natural Science Foundation of Hubei Province (No. ZRZ2015000203), the Technology Creative Project of Excellent Middle & Young Team of Hubei Province (No. T201511), and the Director Fund of the WNLO are acknowledged. The authors thank the Analytical and Testing Center of Huazhong University of Science & Technology and the Center of Micro-Fabrication and Characterization (CMFC) of WNLO for the measurements of the samples.

Notes and references

1 Y. Yang, G. Zheng and Y. Cui, *Chem. Soc. Rev.*, 2013, **42**, 3018–3032.
2 P. Bruce, S. Freunberger, L. Hardwick and J. Tarascon, *Nat. Mater.*, 2012, **11**, 19–29.
3 M. Wild, L. Neill, T. Zhang, R. Purkayastha, G. Minton, M. Marinescub and G. Offer, *Energy Environ. Sci.*, 2013, **42**, 3018–3032.
4 L. Ma, K. Hendrickson, S. Wei and L. Archer, *Nano Today*, 2015, **10**, 315–338.
5 H. Ye, Y. Yin, S. Xin and Y. Guo, *J. Mater. Chem. A*, 2013, **1**, 6602–6608.
6 G. Li, G. Li, S. Ye and X. Gao, *Adv. Energy Mater.*, 2012, **2**, 1238–1245.
7 X. Ji, S. Evers, R. Black and L. Nazar, *Nat. Commun.*, 2011, **2**, 325.
8 J. Li, B. Ding, G. Xu, L. Hou, X. Zhang and C. Yuan, *Nanoscale*, 2013, **5**, 5743–5746.
9 J. Guo, Y. Xu and C. Wang, *Nano Lett.*, 2011, **11**, 4288–4294.
10 B. Zhang, X. Qin, G. Li and X. Gao, *Energy Environ. Sci.*, 2010, **3**, 1531–1537.
11 Z. Li, Y. Jiang, L. Yuan, Z. Yi, C. Wu, Y. Liu, P. Strasser and Y. Huang, *ACS Nano*, 2014, **8**, 9295–9303.
12 C. Lai, Z. Wu, X. Gu, C. Wang, K. Xi, R. Kumar and S. Zhang, *ACS Appl. Mater. Interfaces*, 2015, **7**, 23885–23892.
13 M. Song, Y. Zhang and E. Cairns, *Nano Lett.*, 2013, **13**, 5891–5899.
14 C. Zhang, H. Wu, C. Yuan, Z. Guo and X. Lou, *Angew. Chem., Int. Ed.*, 2012, **124**, 9730–9733.
15 K. Zhang, F. Qin, Y. Lai, J. Li, X. Lei, M. Wang, H. Lu and J. Fang, *ACS Appl. Mater. Interfaces*, 2016, **8**, 60720–66081.
16 H. Peng, J. Liang, L. Zhu, J. Huang, X. Cheng, X. Guo, W. Ding, W. Zhu and Q. Zhang, *ACS Nano*, 2014, **8**, 11280–11289.
17 L. Fei, X. Li, W. Bi, Z. Zhuo, W. Wei, L. Sun, W. Lu, X. Wu, K. Xie, C. Wu, H. Chan and Y. Wang, *Adv. Mater.*, 2015, **27**, 5936–5942.
18 G. Zhou, E. Paek and G. Hwang, *Nat. Commun.*, 2015, **6**, 7760.
19 G. Zhou, L. Yin, D. Wang, L. Li, S. Pei, I. Gentle, F. Li and H. Cheng, *ACS Nano*, 2013, **7**, 5367–5375.
20 H. Hu, H. Cheng, Z. Liu, G. Li, Q. Zhu and Y. Yu, *Nano Lett.*, 2015, **15**, 5116–5123.
21 Y. Qiu, W. Li, W. Zhao, G. Li, Y. Hou, M. Liu, L. Zhou, F. Ye, H. Li, Z. Wei, S. Yang, W. Duan, Y. Ye, J. Guo and Y. Zhang, *Nano Lett.*, 2014, **14**, 4821–4827.
22 G. Li, J. Sun, W. Hou, S. Jiang, Y. Huang and J. Geng, *Nat. Commun.*, 2016, **7**, 10601.
23 Q. Pang, J. Tang, H. Huang, X. Liang, C. Hart, K. Tam and L. Nazar, *Adv. Mater.*, 2015, **27**, 6021–6028.
24 Z. Li, J. Zhang and X. Lou, *Angew. Chem., Int. Ed.*, 2015, **54**, 1–5.
25 C. Hart, M. Cuisinier, X. Liang, D. Kundu, A. Garsuch and L. Nazar, *Chem. Commun.*, 2015, **51**, 2308.
26 Z. Seh, W. Li, J. Cha, G. Zheng, Y. Yang, M. McDowell, P. Hsu and Y. Cui, *Nat. Commun.*, 2013, **4**, 1331.
27 Z. Yang, H. Wang, L. Lu, C. Wang, X. Zhong, J. Wang and Q. Jiang, *Sci. Rep.*, 2016, **6**, 22990.
28 L. Gao, X. Li, H. Hu, G. Li, H. Liu and Y. Yu, *Electrochim. Acta*, 2014, **120**, 231–239.
29 B. Ding, G. Xu, L. Shen, P. Nie, P. Hu, H. Dou and X. Zhang, *J. Mater. Chem. A*, 2013, **1**, 14280–14285.
30 R. Xu, J. Li, J. Lu, K. Amine and I. Belharouak, *J. Mater. Chem. A*, 2015, **3**, 4170–4179.
31 Z. Zhang, Q. Li, S. Jiang, K. Zhang, Y. Lai and J. Li, *Chem.–Eur. J.*, 2015, **21**, 1343–1349.
32 J. Hwang, H. Kim, S. Lee, J. Lee, A. Abouimrane, M. Khaleel, I. Belharouak, A. Manthiram and Y. Sun, *Adv. Energy Mater.*, 2015, **6**, 1501480.
33 Z. Liang, G. Zheng, W. Li, Z. Seh, H. Yao, K. Yan, D. Kong and Y. Cui, *ACS Nano*, 2014, **8**, 5249–5256.
34 B. Ding, L. Shen, G. Xu, P. Nie and X. Zhang, *Electrochim. Acta*, 2013, **107**, 78–84.
35 A. Ramadoss and S. Kim, *Carbon*, 2013, **63**, 434–445.
36 Z. Xiao, Z. Yang, L. Wang, H. Nie, M. Zhong, Q. Lai, X. Xu, L. Zhang and S. Huang, *Adv. Mater.*, 2015, **27**, 2891–2898.
37 K. Cao, J. Lu, H. Li, Y. Shen and M. Wang, *RSC Adv.*, 2015, **5**, 62630–62637.
38 D. Huang, B. Zhang, Y. Zhang, F. Zhan, X. Xu, Y. Shen and M. Wang, *J. Mater. Chem. A*, 2013, **1**, 1415–1420.
39 D. Long, W. Li, L. Ling, J. Miyawaki, I. Mochida and S. Yoon, *Langmuir*, 2010, **26**, 16096–16102.
40 Z. Li, J. Zhang, Y. Chen, J. Li and X. Lou, *Nat. Commun.*, 2015, **6**, 8850.
41 Z. Li, C. Li, X. Ge, J. Ma, Z. Zhang, Q. Li, C. Wang and L. Yin, *Nano Energy*, 2016, **23**, 15–26.
42 C. Tang, B. Li, Q. Zhang, L. Zhu, H. Wang, J. Shi and F. Wei, *Adv. Funct. Mater.*, 2016, **26**, 577–585.

43 J. Jiang, J. Zhu, W. Ai, X. Wang, Y. Wang, C. Zou, W. Huang and T. Yu, *Nat. Commun.*, 2015, **6**, 8622.
44 W. Li, Z. Liang, Z. Lu, H. Yao, Z. Seh, K. Yan, G. Zheng and Y. Cui, *Adv. Energy Mater.*, 2015, **5**, 1500211.
45 L. Gao, R. Liu, H. Hu, G. Li and Y. Yu, *Nanotechnology*, 2014, **25**, 175402–175410.
46 H. Wang, H. Yang, L. Lu, Y. Zhou and Y. Wang, *Dalton Trans.*, 2013, **42**, 8781–8787.
47 X. Niu, X. Wang, D. Xie, D. Wang, Y. Zhang, Y. Li, T. Yu and J. Tu, *ACS Appl. Mater. Interfaces*, 2015, **7**, 16715–16722.
48 S. Talapaneni, T. Hwang, S. Je, O. Buyukcakir, J. Choi and A. Coskun, *Angew. Chem., Int. Ed.*, 2016, **128**, 3158–3163.
49 L. Gao, S. Li, D. Huang, Y. Shen and M. Wang, *J. Mater. Chem. A*, 2015, **3**, 10107–10113.
50 L. Gao, S. Li, D. Huang, Y. Shen and M. Wang, *Electrochim. Acta*, 2015, **182**, 529–536.
51 L. Gao, D. Huang, Y. Shen and M. Wang, *J. Mater. Chem. A*, 2015, **3**, 23570–23576.
52 Q. Sun, B. He, X. Zhang and A. Lu, *ACS Nano*, 2015, **9**, 8504–8513.
53 Y. Fu, Q. Wei, B. Lu, X. Wang and S. Sun, *J. Alloys Compd.*, 2016, **684**, 419–427.
54 L. Pan, Y. Liu, X. Xie, X. Ye and X. Zhu, *Nano Res.*, 2016, **9**, 2057–2069.
55 Z. Lu, C. Yip, L. Wang, H. Huang and L. Zhou, *ChemPlusChem*, 2012, **77**, 991–1000.
56 C. Wang, F. Wang, Y. Zhao, Y. Li, Q. Yue, Y. Li, Y. Liu, A. Elzatahry, A. Enizi, Y. Wu, Y. Deng and D. Zhao, *Nano Res.*, 2016, **9**, 165–173.